

Interferometer predictions with triangulated images: solving the multi-scale problem

C. Brinch¹ ^{*} and C. P. Dullemond^{2,3}

¹Centre for Star and Planet Formation (*Starplan*) and Niels Bohr Institute

University of Copenhagen, Juliane Maries Vej 30, 2100 Copenhagen Ø, Denmark

²Institut für Theoretische Astrophysik Zentrum für Astronomie der Universität Heidelberg

Albert-Ueberle-Str. 2, 69120 Heidelberg, Germany

³Max-Planck-Institute für Astronomie Königstuhl 17, 69117 Heidelberg, Germany

4 October 2018

ABSTRACT

Interferometers play an increasingly important role for spatially resolved observations. If employed at full potential, interferometry can probe an enormous dynamic range in spatial scale. Interpretation of the observed visibilities requires the numerical computation of Fourier integrals over the synthetic model images. To get the correct values of these integrals, the model images must have the right size and resolution. Insufficient care in these choices can lead to wrong results. We present a new general-purpose scheme for the computation of visibilities of radiative transfer images. Our method requires a model image that is a list of intensities at arbitrarily placed positions on the image-plane. It creates a triangulated grid from these vertices, and assumes that the intensity inside each triangle of the grid is a linear function. The Fourier integral over each triangle is then evaluated with an analytic expression and the complex visibility of the entire image is then the sum of all triangles. The result is a robust Fourier transform that does not suffer from aliasing effects due to grid regularities. The method automatically ensures that all structure contained in the model gets reflected in the Fourier transform.

Key words: Techniques: image processing, Techniques: interferometric

1 INTRODUCTION

The technique of interferometry has a long history in radio astronomy and gains more and more popularity also at other wavelengths. In the millimetre and sub-millimetre domain arrays such as the SMA, Plateau de Bure and CARMA allow, for instance, young stellar objects and protoplanetary disks to be spatially resolved down to a few tens of AU. And soon, ALMA will achieve few-AU resolution at wavelengths ranging from 0.3 to 3 mm. In the mid- and near-infrared optical interferometry is maturing as well and has provided new insights into the physics of protoplanetary disks and active galactic nuclei. The interpretation of these data, however, often requires detailed comparisons with theoretical models. Typically a radiative transfer model is produced of the object of interest, and the results compared to the observations. This paper is about this process of comparing models to interferometric measurements.

Interferometers probe the image of the object on the sky in the Fourier plane. Rather than measuring pixel-by-pixel

intensities and thus immediately yielding an image for the observer to interpret, in radio and millimeter interferometry each pair of telescopes measures the so-called 'complex visibility' (the normalized correlation function between the signals measured by the two telescopes). In optical and infrared interferometers usually only the amplitude (not the phase) of the visibility is measured, which is in fact the ratio of the correlated flux density to the total flux density. According to the van Cittert-Zernike theorem the complex visibility as a function of baseline coordinates (u, v) is equal to the Fourier transform of the image on the sky divided by its total flux density. For each combination of three telescopes one can measure a "closure phase" which also directly follows from the complex Fourier values belonging to each telescope pair. Interferometry measurements are thus measurements in Fourier space, usually called the uv-plane. If sufficient baselines are available, i.e., the uv-plane is sufficiently well covered, then the inverse Fourier transform can be carried out and an image reconstructed. However, often the uv-plane is sparsely covered and image reconstruction is non-unique. In such cases, any model comparison will have to take place in the uv-plane itself, and model images must be Fourier transformed to the uv-plane before comparison

^{*} E-mail: brinch@nbi.dk

can take place. Also for the case of a high uv-coverage, this “forward method” (adapting the model to the observations) can also be useful for predicting the feasibility of observing particular objects and phenomena.

In some cases where the astronomical source has a simple structure which can adequately be described by an algebraic expression (e.g., point, sphere, disk, cylinder, ring, etc.), the complete Fourier transform is easily calculated analytically and used to model the data (Pearson 1999; Martí-Vidal et al. 2014). However, if a numerical model (typically the output from a radiative transfer code) is used to describe the source, the Fourier transform needs to be calculated numerically. The task of numerically calculating a Fourier transform of a model image may seem trivial. Algorithms such as Fast Fourier Transform (FFT) can do this with high precision and speed. It turns out, however, that for models that involve a large dynamic range in spatial scale this task can be difficult. For example, the problem of a collapsing molecular cloud core of 10^4 AU size, with a proto-stellar disk inside of 100 AU size which surrounds a protostar of 0.1 AU size covers already 5 orders of magnitude in spatial scale. Although current interferometers are not able to observe all of these scales simultaneously, it is still possible to cover 2-3 orders of magnitude in spatial scale with ALMA. Observations of a molecular line and the dust continuum will record large scale emission in the line centre and small scale emission in the line wings and surrounding continuum. Calculating the uv-plane image is then not trivial at all, and doing so without great care will inevitably lead to errors. For example, one would need to use sufficient padding with blank space around the source model in order to avoid mirror images in the Fourier transform. In this paper we will describe a new method of computing synthetic uv-plane “observations” which are extremely robust and yield proper results without much care. The method we present can easily be implemented into existing radiative transfer codes or it can be made into a stand-alone subroutine that can post-process the output from ray-tracing codes. All examples of the method presented in this paper have been made using a customised parallel version of the public available LIME code (Brinch & Hogerheijde 2010).

2 UNSTRUCTURED IMAGES

The main idea of our method is to provide model images not as “raster images” (Fig. 1-left) but as “unstructured grid images” (Fig. 1-right).

Normally when one makes model images one computes the intensity on a regular rectangular grid (a raster), like a normal digital photo. One thus obtains a list of intensities as a function of x - and y - integer positions: $I_{i,j}$ with $1 \leq i \leq N_x$ and $1 \leq j \leq N_y$ where $N_x N_y$ is the total number of pixels. Each such intensity belongs to location (x_i, y_j) on the image where $x_i = x_0 + i\Delta x$ and $y_j = y_0 + j\Delta y$, where Δx and Δy determine the spatial resolution. Usually $\Delta x = \Delta y$. The largest spatial scale that can be sampled with such images is $N_x \Delta x$ in x-direction and $N_y \Delta y$ in y-direction. The smallest spatial scale is Δx in x-direction and Δy in y-direction. When making such an image for a model that covers a large dynamic range in spatial scale one must choose Δx , Δy small enough and N_x and N_y large enough to

encompass all these scales. In fact, when computing a meaningful Fourier transform for interferometry one must make sure that $N_x \Delta x$ and $N_y \Delta y$ are *substantially larger* than the largest scales you can pick up with your interferometer. This is because FFT assumes cyclic symmetry in x and y (leading to mirror copies of your image at regular intervals) whereas in reality this is not true. A proper Fourier transform thus always requires large enough N_x and N_y , even for a single baseline. If one wishes to make *one* image for multiple baselines then this puts even stronger lower limits to N_x and N_y . In any event, one always has to take extreme care to choose Δx , Δy , N_x and N_y properly.

The idea we propose here is to produce images on an “unstructured grid” in the image plane (Fig. 1-right). This sounds much more complex than it actually is. The user of our method must generate a set of points (x_i, y_i) on the image plane (Fig. 1-upper-right), compute the intensity $I_{\nu,i}$ corresponding to each of these points, and provide the set $(x_i, y_i, I_{\nu,i})$ for $1 \leq i \leq N$, as well as a set of uv-spacings corresponding to the telescope baselines of interest. Our algorithm will then generate a proper triangulation (Fig. 1-lower-right), and compute the complex visibility values for each baseline, as we shall describe in the next section. The only thing the user must take care of is to assure that the set of image grid points (x_i, y_i) properly map the entire model. Regions where there are small-scale structures require a denser sampling than regions of large scale smooth structures. If we take the example of a collapsing molecular cloud core with a central star+disk again one should assure that there are sufficient points probing the very small (100 AU) disk and an equally large number of points covering the large (10000 AU) scale infalling envelope. If one randomly places points with a probability distribution such that there are statistically as much points between 1 and 100 AU as there are between 100 and 10000 AU, then one has presumably a proper sampling. An example of such a probability distribution is

$$P(r)dr \propto \frac{dr}{r} \quad (1)$$

normalised such that

$$\int_{r_{\text{in}}}^{r_{\text{out}}} P(r)dr = 1. \quad (2)$$

In principle one can also make more regular arrangements of pixels with this scheme which also resolve all spatial scales properly, see e.g. Fig. 2.

The optimal solution is to have a line of sight pass through each model grid cell. For a regular $N_x N_y$ computational grid (in 2D) this would result in the traditional raster image. However, for an AMR style refined grid, the resulting intensity point distribution would be similar to that of Fig. 2. In 3D codes which already make use of a randomly sampled grid, e.g., LIME, one would simply trace a line of sight for each grid point position projected onto the image plane. This automatically ensure that all structure of the model is probed by the ray-tracer.

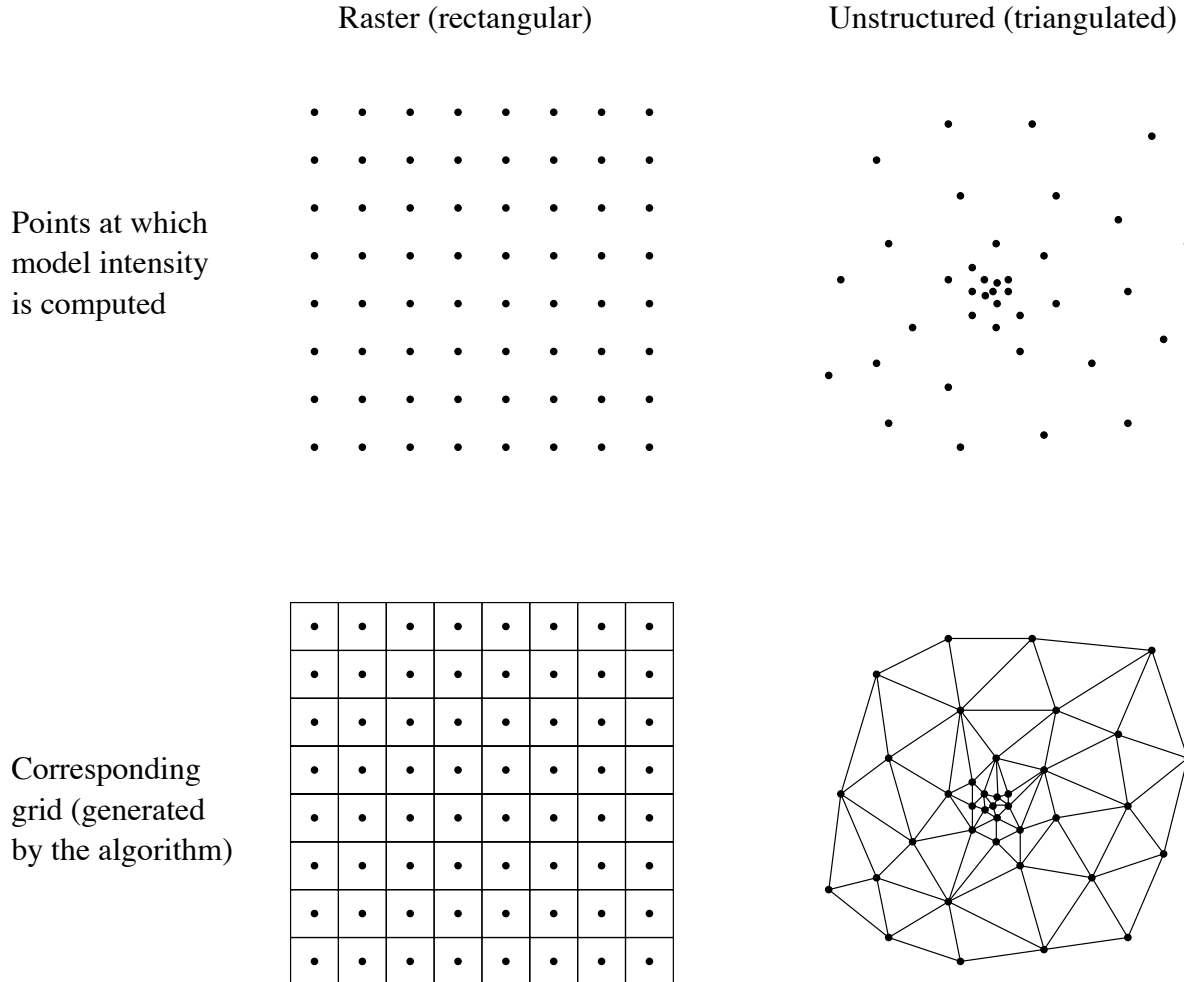


Figure 1. Schematic comparison of standard image pixel arrangement (left) and our unstructured pixel arrangement (right). The dots are the locations where the intensity I_{ν} is given (upper panels). For the standard pixel arrangements these correspond to the average values of square pixels, i.e. the dots are located in the middle of their pixel (lower left). For our unstructured pixel arrangements the dots are the corners of triangular “pixels”. The intensity I_{ν} is linearly interpolated inside each triangle. The user of our algorithm only needs to provide the coordinates in the image plane of a set of points and their corresponding I_{ν} values (upper right). The algorithm will then produce the corresponding triangulation (lower right) automatically.

3 COMPUTING THE FOURIER TRANSFORM

Once a set of intensities $I_{\nu,i}$, whether structured or unstructured, has been obtained, our algorithm will calculate the visibilities.

The first step of the algorithm calculates the Delaunay triangulation of the point set (x_i, y_i) . The Delaunay triangulation is defined as the triangulation in which none of the points (x_i, y_i) lies inside any of the triangle circumcircles. The resulting triangulation has an intensity measurement at each triangle vertex. These triangles are the equivalent to the pixels in a raster map and we will refer to them as triangular pixels or *trixels*. An example of the Delaunay triangulation is shown in the lower right panel of Fig. 1. Algorithms for constructing the Delaunay triangulation are readily available in many scientific computation packages, and we use the Matplotlib¹ Delaunay procedure. Any other similar tool, such as IDLs TRIANGULATE or the command line

tool QHULL (Barber et al. 1996) can be used as well. One can also write custom triangulation code, for instance based on the method by Lee & Schachter (1980). An extensive discussion on how to implement Delaunay triangulations can be found in Springel (2010). Throughout the remainder of this section we refer the reader to Fig. 3, showing the geometry of a *trixel*.

The two-dimensional Fourier transformation of an intensity distribution $I(x, y)$ is given by

$$F(\mathbf{w}) = \iint_{-\infty}^{\infty} I(\mathbf{r}) e^{-i(\mathbf{w} \cdot \mathbf{r})} d\mathbf{r}, \quad (3)$$

where $\mathbf{w} = u\hat{\mathbf{x}} + v\hat{\mathbf{y}}$ and $\mathbf{r} = x\hat{\mathbf{x}} + y\hat{\mathbf{y}}$. We can split the Fourier transform into a sum of Fourier transforms of the individual triangles because of the linearity of the transformation. Thus the task is reduced to calculating the Fourier transform of a single three sided polygon. If we at first make the simplifying assumption that $I(x, y)$ is constant over the face of the triangle, e.g., by using the (weighted) mean of

¹ <http://matplotlib.org>

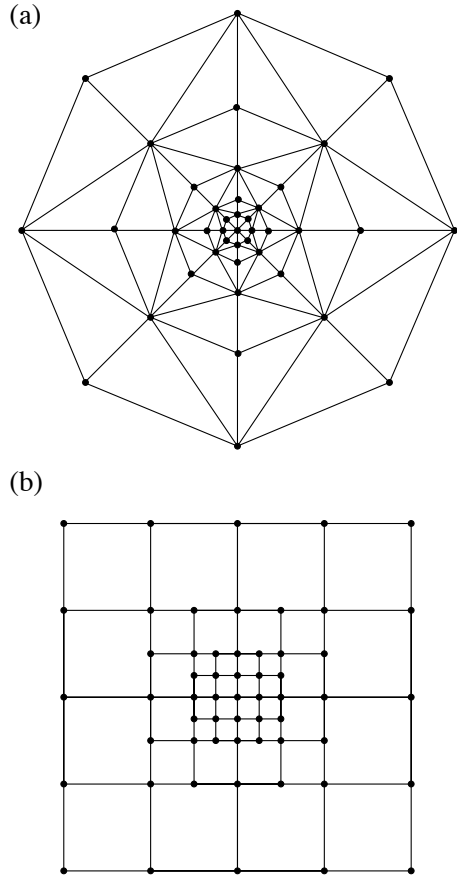


Figure 2. With the general formalism of unstructured grids (i.e. specifying a set $(x_i, y_i, I_{\nu,i})$ for $1 \leq i \leq N$) one can also produce regular grids that still resolve spatial scales properly. For centrally condensed systems such as protoplanetary/proto-stellar disks or collapsing clouds onto single stars one could arrange the pixels in circles (upper). For more general clumpy media one could use a patch-style grid (lower). The danger with these grid is, however, that the regularity could lead to dangerous “aliasing” effects, in particular with the patch-style gridding. A semi-random ordering of points as in Fig. 1-right is always safer and is preferred if possible.

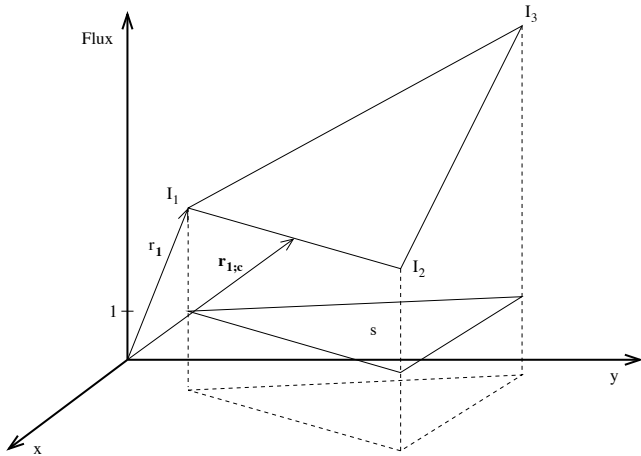


Figure 3. The geometry of a trixel as used throughout Sec. 3.

the three intensity values of the triangle vertices, we can follow the derivation in Houshmand et al. (1991) to obtain the solution

$$F_{\Delta}(\mathbf{w}) = \sum_{n=1}^3 I_{\Delta} \frac{\hat{\mathbf{z}} \times \mathbf{l}_n \cdot \mathbf{l}_{n-1}}{(\mathbf{w} \cdot \mathbf{l}_n)(\mathbf{w} \cdot \mathbf{l}_{n-1})} e^{-i(\mathbf{w} \cdot \mathbf{r}_n)} \quad (4)$$

where Δ denotes a single triangle with vertex coordinate vectors \mathbf{r}_n and $\mathbf{l}_n = \mathbf{r}_{n+1} - \mathbf{r}_n$ is the vector along the n 'th edge. The vertices and edges are enumerated counter clockwise. We then obtain the Fourier transform of the entire image by summing over all triangles,

$$F(\mathbf{w}) = \sum_{all \Delta} F_{\Delta}(\mathbf{w}). \quad (5)$$

This formula is simple to work with and gives a good representation of the image in uv-space, but it does assume a single averaged value for each triangle. If the underlying model gets properly sampled by a ray-tracer, the intensity can be assumed to vary linearly between the vertices of the triangles and therefore we can assume that the face of a triangle is described by a plane spanned by the intensity at each of the three vertices. Now in order to introduce a linear variation of the intensity over the face of a triangle, we note that the following distribution over the triangular patch describes the plane spanned by the intensity values at the vertices,

$$I(\mathbf{r}) = \sum_{n=1}^3 I_n \frac{\hat{\mathbf{z}} \times \mathbf{l}_{n+1} \cdot (\mathbf{r} - \mathbf{r}_{n+1})}{2A} s(\mathbf{r}), \quad (6)$$

where A is the area and s is the shape function of the triangle,

$$s(\mathbf{r}) = \begin{cases} 1, & \mathbf{r} \in \Delta \\ 0, & \text{otherwise} \end{cases} \quad (7)$$

By inserting Eq. 6 into Eq. 3, we get the expression for the Fourier transform of the triangular patch

$$F(\mathbf{w}) = \sum_{n=1}^3 I_n \frac{\hat{\mathbf{z}} \times \mathbf{l}_{n+1}}{2A} \cdot \iint_{\Delta} (\mathbf{r} - \mathbf{r}_{n+1}) e^{-i(\mathbf{w} \cdot \mathbf{r}_n)} dA, \quad (8)$$

where the shape function has been eliminated by letting the domain of the integral be the support of triangular patch. The solution to the integral part of Eq. 8 is derived in McInturff & Simon (1991) and we will proceed to quote the resulting expression

$$\begin{aligned} \iint_{\Delta} (\mathbf{r} - \mathbf{r}_{n+1}) e^{-i(\mathbf{w} \cdot \mathbf{r}_n)} dA = \\ \frac{1}{|\mathbf{w}|^2} \sum_{m=1}^3 e^{-i(\mathbf{w} \cdot \mathbf{r}_{m;c})} \\ \cdot \left\{ \left[\hat{\mathbf{z}} \times \mathbf{l}_m + \left(i\mathbf{r}_{m;c} - i\mathbf{r}_{n+1} - \frac{2\mathbf{w}}{|\mathbf{w}|^2} \right) \hat{\mathbf{z}} \cdot \mathbf{l}_m \times \mathbf{w} \right] \right. \\ \left. j_0 \left(\frac{\mathbf{w} \cdot \mathbf{l}_m}{2} \right) - \mathbf{l}_m \frac{\hat{\mathbf{z}} \cdot \mathbf{l}_m \times \mathbf{w}}{2} j_1 \left(\frac{\mathbf{w} \cdot \mathbf{l}_m}{2} \right) \right\} \end{aligned} \quad (9)$$

$\mathbf{r}_{m;c}$ denotes the centre point of the m 'th edge and j_0 and j_1 are the Bessel functions of the first kind of order 0 and 1, respectively. Again we obtain the Fourier transform of the entire image by summing over all individual triangles. Equation 8 gives us a *complete* set of visibilities from which we can select a subset that corresponds to a set of observed u, v -points or we can predict the interferometer response at different antenna configurations and integration times. This Fourier transform does not suffer from aliasing due to the regularity of the pixels since the triangles are randomly oriented (unless, of course, the triangle vertices are sampled at regular intervals) and we do not need a taper region to avoid mirror copies of the image which is needed when using FFT because FFT assumes periodic boundary conditions. The resulting Fourier components can easily be stored in the standard uv-FITS format (Hanisch et al. 2001). The drawback of the Fourier transform (8) is that it is not fast to compute. The method presented here takes $O(N \times M)$ operations, where $M \leq N$, while FFT can be carried out in $O(N \log N)$ operations.

4 COMPARISON OF METHODS

First we show the Fourier transform of two simple shapes, a circular annulus (Fig. 4) and an inclined rectangle (Fig. 5). Both shapes have been imaged on a 50×50 ($=2500$) pixel raster map as well as on a 2500 point trixel map. The resulting images are shown in the left column of Fig. 4 and 5. The points for the trixel images have been chosen so that most of the points fall inside the shape and just across the edge. In fact, for the rectangle, only the edge has been mapped with a high density of points, whereas the constant inside and outside of the rectangle has a relatively low point density. The result is a very clearly defined shape for both the annulus and the rectangle as compared to the raster version where the edge appears rough (or indeed, pixelated). We have furthermore used anti-aliasing with 16 rays per pixel in the raster version of the rectangle in order to smooth out the edges. This means that the pixels along the edges are coloured according to the fraction of rays that are randomly sampled within each pixel that falls inside the rectangle. This anti-aliasing requires an additional 800 rays. When deciding where to place the rays for the triangulated images, it is generally not possible to do emission weighted ray-tracing, since the regions of strong emission are not known a priori. However, if the source structure is known, at least to a certain degree (which is the case for the rectangle and annulus cases shown here), one can place rays accordingly. When using the LIME code, the positions of the grid points are already weighted by the source structure and the projection of the grid points can then be used as a proxy for the distribution of the rays. Many ray-tracing codes already make use of some sort of “clever” ray placement (e.g., Dullemond & Turolla 2000; Pontoppidan et al. 2009) from which a triangulated image could be formed rather than remapping the rays onto a raster image.

The right column of Fig. 4 and 5 shows the corresponding Fourier transforms, FFT in the case of the raster images and the method derived above in the case of the trixel images. It is clear that for both cases, the two different Fourier transformation methods produce basically the

same result, but because our method is not resolution limited, the resulting Fourier transform comes out in a much, much higher resolution (actually higher than what can be displayed in a raster contour plot). The FFT of the annulus shows clear asymmetric edge effects which are completely absent in trixel Fourier transform. The anti-aliasing which is used to smooth out the edges in the rectangle example of Fig. 5 does not improve the FFT significantly.

The next example is a more realistic case, an astronomical pseudo-model, based on a real protoplanetary disk model, with the addition of an arbitrary spiral density perturbation. The spiral was chosen in order to introduce spatial variations on all scales and is in no way assumed to describe any physical reality, hence pseudo-model. However, the underlying disk model is consistent with current models of the disk around the T Tauri star TW Hydra (as described in, e.g., Andrews et al. (2012)) in terms of mass, mass distribution, size, distance, temperature, etc. The radiation transfer model has been calculated by the LIME code and the solution has been ray-traced to produce an image of the continuum at 1 mm. Figure 6 shows the resulting raster image and trixel image. The resolution and image size of the raster image has been chosen to minimize the artifacts in the visibilities which can be measured by ALMA, given a source distance of 50 parsec, assuming a synthesized beam size of 0.1 arcsec and a maximum recoverable scale of 15 arcsec. The resulting raster image consists of $10^3 \times 10^3$ pixels. The trixel image is made out of as few as possible rays, and hence trixels, which still produces a Fourier transform which is as good as the FFT. In this case the number of rays are 5000 or a factor of 200 fewer rays than what is needed for the raster image. If we use fewer rays for the trixel image the Fourier transform no longer compares well to the FFT. This, however, is not due to a limitation of the method, but simply because we no longer describe the source structure well enough. An important thing to notice is that, despite the fewer rays used in the trixel image, we can trace the spirals in the Fourier transform to much greater uv-distances, although the spiral do tend to become noisier.

Comparing the Fourier transforms, we see that there is quite some difference between the FFT and our method. A test shows that if raster images are made in progressively higher resolution, the FFT approaches the Fourier transform produced by our method, and so the morphologic difference the two Fourier transforms shown here are only due to the inadequate resolution in the raster image.

Finally, we have made a small resolution study of our method and compared this with the performance of the FFT. For this, we used a 2D unit disk which has the well-known analytic Fourier transform,

$$F(u, v) = \frac{j_1(2\pi\sqrt{u^2 + v^2})}{\sqrt{u^2 + v^2}}. \quad (10)$$

The unit disk has been mapped onto a regular pixel grid, using anti-aliasing, that is, with a fractional shading of pixels proportionally to the fraction of the pixel area that is covered by the disk. For the trixel version, the unit disk has been mapped similarly to the example in Fig. 4.

The result of the resolution study is shown in Fig 7, where the full red curve shows the analytic solution and the dotted blue and dashed green curves show the trixel method

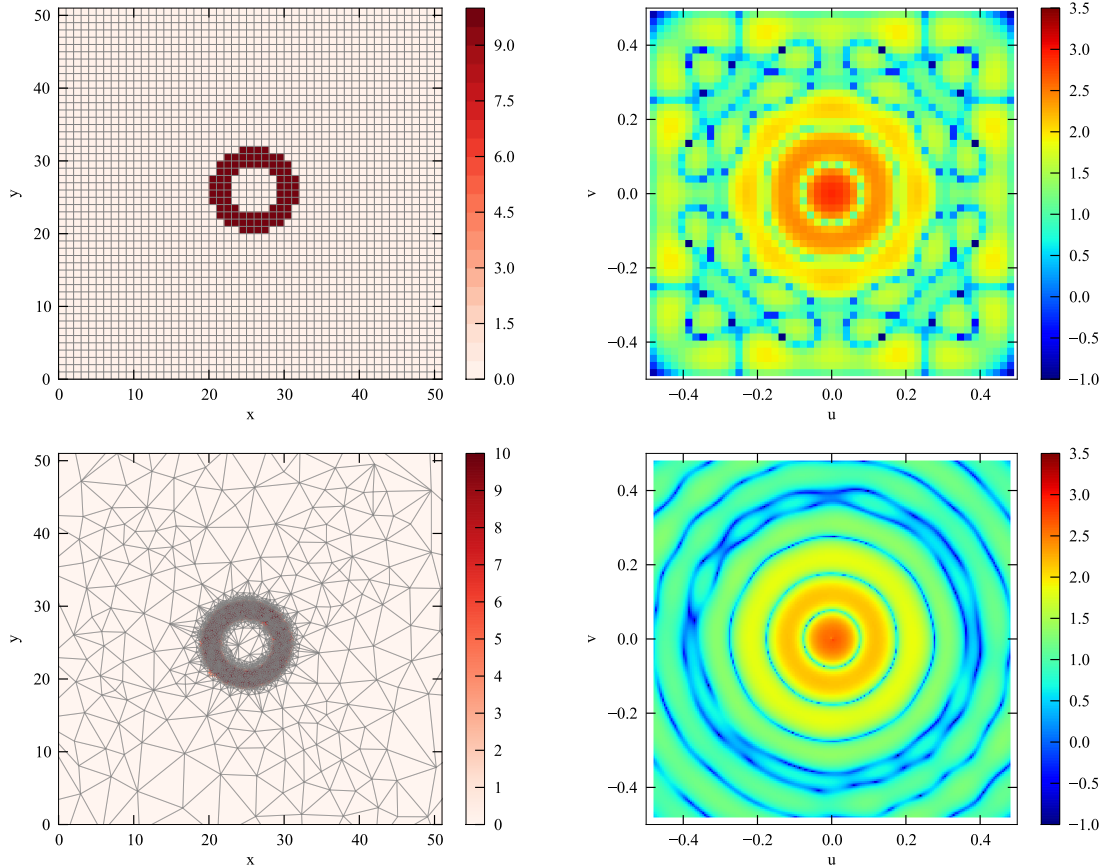


Figure 4. The figure shows an image of an annulus (left) and the corresponding Fourier amplitudes (right). In the top row, a normal FFT algorithm has been applied to a regular pixel image, whereas in the bottom row, the method presented in this paper has been applied to an irregular triangulated image.

and FFT respectively. The left panel shows the solutions at a resolution of 30^2 pixels for the FFT version and 30^2 rays for the trixel method. The right panel in Fig. 7 shows the L^2 norm (the Euclidean distance between solutions) of both methods as a function of increasing resolution. Both methods seem to have converged at around $N = 30$. After convergence, the L^2 norm of FFT is slightly better than the trixel method, but judged by the fit in the main panel, both methods give very accurate results. The phase is slightly offset for larger uv-spacings in the trixel method, but on the other hand, the FFT over-produces the power by a small amount on the smallest spatial scales and obviously, the FFT method has a significantly lower resolution in uv-space than what can be achieved by the method presented here.

5 CONCLUSIONS

In this paper we have presented a method to create radiative transfer model images in arbitrary resolution and very high dynamic range using a finite, and much smaller number of rays than is needed for a raster image in comparable resolu-

tion. The method uses an unstructured (possibly random) distribution of rays out of which a Delaunay triangulation is calculated. Each Delaunay triangle is easily Fourier transformed using Eq. 8.

Unfortunately, Eq. 8 becomes very time consuming for large or “complete” sets of uv-spacings. The Fourier transformation method presented here requires $O(N^2)$ operations which from a performance point of view is vastly outperformed, particularly for large N , by FFT which requires $O(N \log N)$ operations. However, like Eq. 8, ray-tracing in a 3-D radiative transfer model is also an $O(N^2)$ process in the number of pixels per axis and so what is gained in speed from using FFT is quickly lost again from the increased ray-tracing time in order to reach high enough image resolution. One could consider taking an unstructured, and therefore high-resolution, set of rays and remap it onto a very high resolution raster in order to perform an FFT. Such a remapping, however, can potentially also be quite time consuming on its own and it still requires a somewhat arbitrary choice of minimum and maximum scale to be made. Increasing the number of pixels dramatically has the further disadvantage

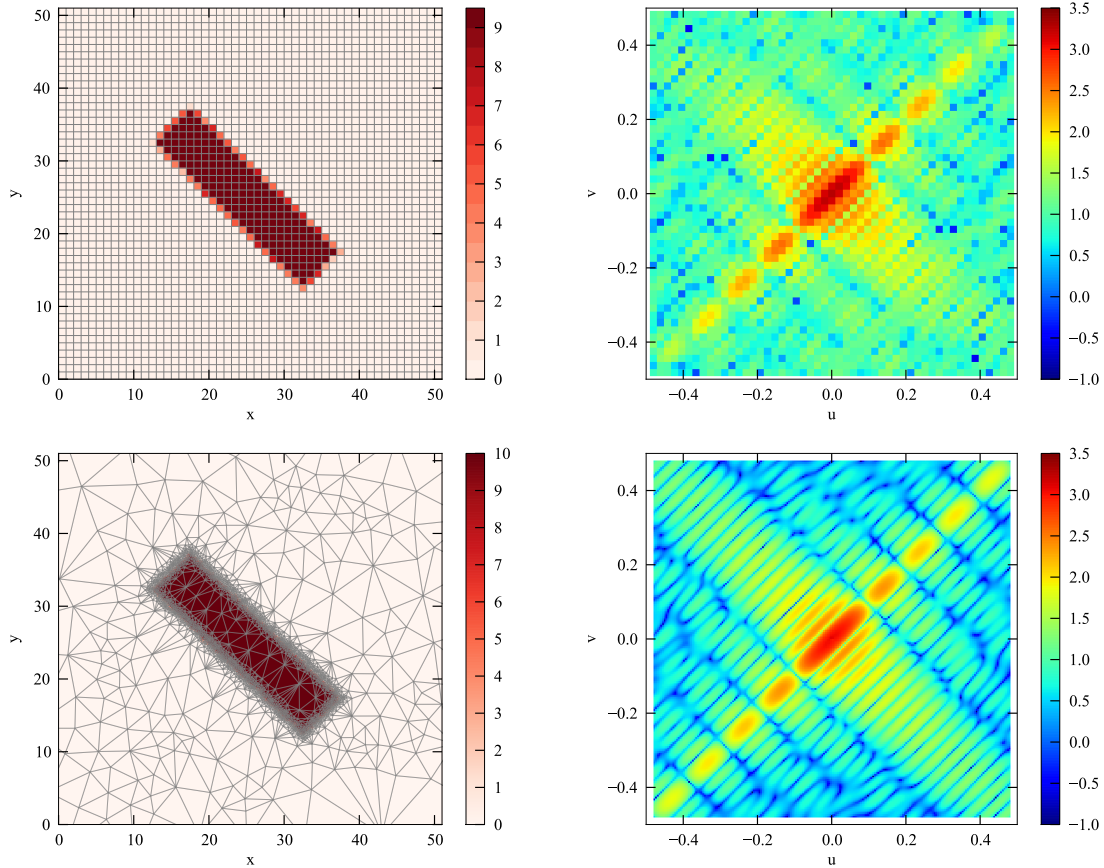


Figure 5. Similar to Fig. 4, but for a rectangular shape function. In this example we have used anti-aliasing on the raster image in order to smooth out the sharp edges and minimize the artefacts due to the staircase effect of the square pixels.

of producing very large FITS files, in particular when doing spectral line images, where the spectral axis can potentially hold hundreds of channels. For the example in Fig 6, the FFT on the raster image is done in less than a few seconds (which means that the computation time is dominated by I/O and other overhead), whereas the Fourier transform on the trixel image takes a total of 1.5 minutes. However, this Fourier transform has about four times higher resolution than the FFT. In order to reach the same resolution in uv-space with FFT, the image has to be ray-traced at four times the resolution. The FFT operation on the higher resolution raster image does not take noticeable longer, but the ray-tracing time, in this example, goes from about 20 seconds to about 4 minutes and this does not include the additional time requirement when adding anti-aliasing in order to improve the image quality. It is also possible to lower the computation time significantly for the unstructured Fourier transform method, when comparing a model to interferometric data, by only calculating the uv-points which corresponds to the observed uv-spacings, rather than calculating complete sets of uv-points. Equation 5 is also trivially parallelisable which helps to speed up the calculations since most modern computers have multiple cores.

There is currently no image container for unstructured triangulated images although the FITS format could in principle be used. One option would be to build the Fourier transformer directly into the ray-tracing code and let the code output a uv-FITS file rather than having the Fourier transformation be a post-processing tool that works on outputted images. Alternatively, trixels can be stored in standard FITS format as tabulated data.

REFERENCES

- Andrews S. M., Wilner D. J., Hughes A. M., Qi C., Rosenfeld K. A., Oberg K. I., Birnstiel T., Espaillat C., Cieza L. A., Williams J. P., Lin S.-Y., Ho P. T. P., 2012, ApJ, 744, 162
- Barber C. B., Dobkin D. P., Huhdanpaa H., 1996, ACM Trans. Math. Software, 22, 469
- Brinch C., Hogerheijde M. R., 2010, A&A, 523, 25
- Dullemond C. P., Turolla R., 2000, A&A, 360, 1187
- Hanisch R. J., Farris A., Greisen E. W., Pence W. D.,

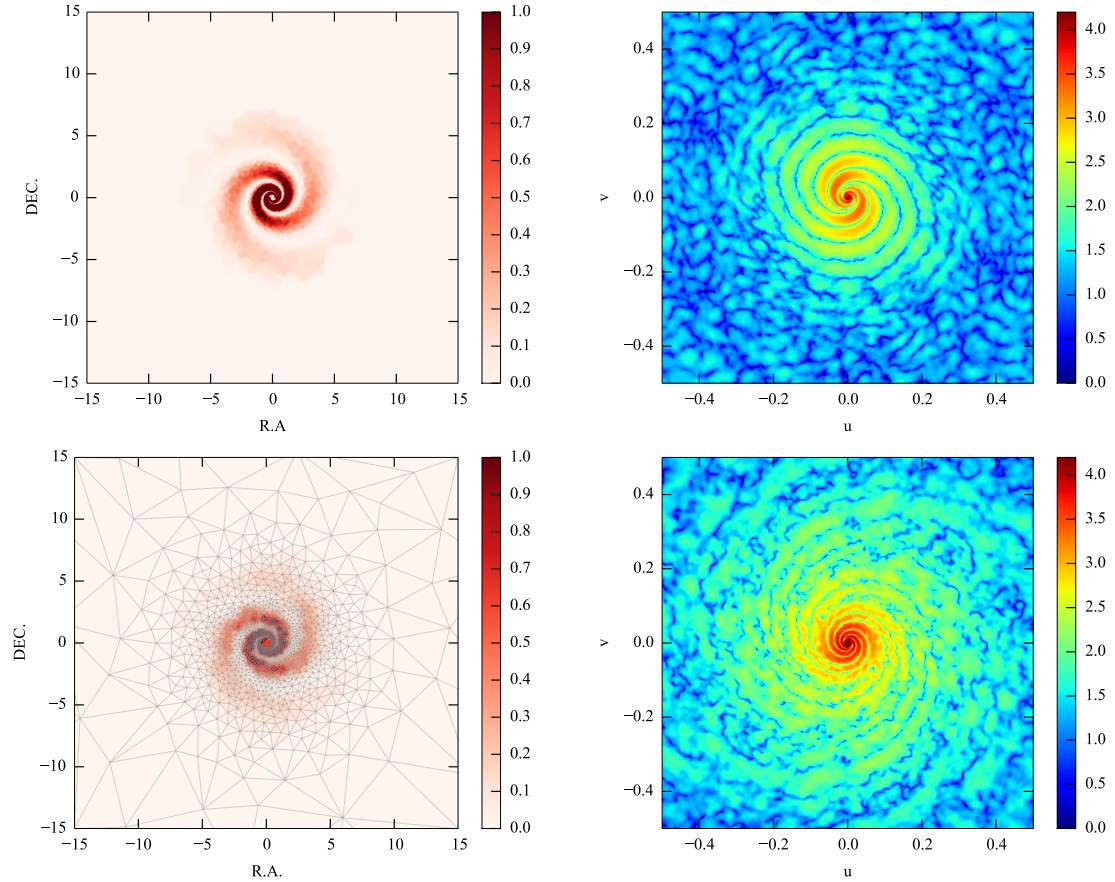


Figure 6. Similar to Fig. 4 but for a radiative transfer model of a toy disk model.

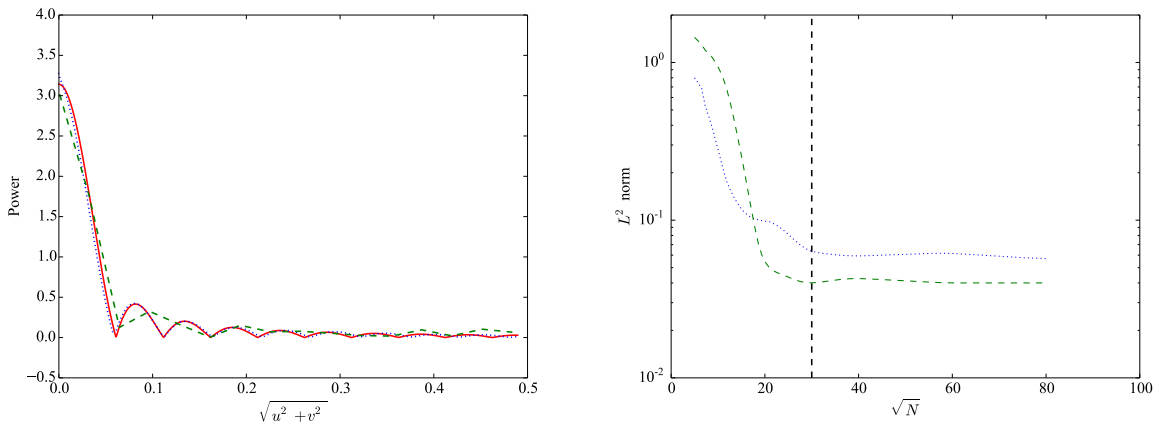


Figure 7. The left panel shows a comparison between the analytic Fourier transform of a unit disk (full red line) and the results of FFT (dashed green) and the trixel method (dotted blue). The right panel shows the L^2 norm of both methods as function of resolution. N refers to the number of pixels in the case of FFT and the number of rays in the case of the trixel method.

- Schlesinger B. M., Teuben P. J., Thompson R. W.,
Warnock A. I., 2001, A&A, 376, 359
- Houshmand B., Chew W. C., Lee S.-W., 1991, IEEE Transactions on Antennas and Propagation, 39, 252
- Lee D. T., Schachter B. J., 1980, Internat. J. Comput. Inform. Sci., 9, 219
- McInturff K., Simon P., 1991, IEEE Transactions on Antennas and Propagation, 39, 1441
- Marti-Vidal I., Vlemmings W. H. T., Muller S., Casey S., 2014, arXiv, p. 4984
- Pearson T. J., 1999, in Taylor G. B., Carilli C. L., Perley R. A., eds, Synthesis Imaging in Radio Astronomy II Non-Imaging Data Analysis. p. 335
- Pontoppidan K. M., Meijerink R., Dullemond C. P., Blake G. A., 2009, ApJ, 704, 1482
- Springel V., 2010, MNRAS, 401, 791